Combining shape and intensity dxa-based statistical approaches for osteoporotic HIP fracture risk assessment

COMBINING SHAPE AND INTENSITY DXA-BASED STATISTICAL APPROACHES FOR OSTEOPOROTIC HIP FRACTURE RISK ASSESSMENT

Alessandra Aldieri[1,2], Mara Terzini[1,2], Alberto L. Audenino[1,2],

Cristina Bignardi[1,2], Umberto Morbiducci[1,2]

[1] Department of Mechanical and Aerospace Engineering, Politecnico di Torino, Turin, Italy

[2] Polito[BIO]Med Lab, Politecnico di Torino, Turin, Italy

ORCID list

A. Aldieri: 0000-0002-2397-3353

M. Terzini: 0000-0002-5699-6009

A. Audenino: 0000-0002-4877-3630

C. Bignardi: 0000-0002-7065-2552

U. Morbiducci: 0000-0002-9854-1619

CORRESPONDING AUTHOR:

Umberto Morbiducci

PoliToBIOMed Lab

Department of Mechanical and Aerospace Engineering - Politecnico di Torino

Corso Duca degli Abruzzi, 24 – 10129 Torino Italia

e-mail: umberto.morbiducci@polito.it

ABSTRACT

Aiming to improve osteoporotic hip fracture risk detection, factors other than the largely adopted Bone Mineral Density (BMD) have been investigated as potential risk predictors. In particular Hip Structural Analysis (HSA)-derived parameters accounting for femur geometry, extracted from Dual-energy X-ray Absorptiometry (DXA) images, have been largely considered as geometric risk factors. However, HSA-derived parameters represent discrete and cross-correlated quantities, unable to describe proximal femur geometry as a whole and tightly related to BMD. Focusing on a post-menopausal cohort (N=28), in this study statistical models of bone shape and BMD distribution have been developed to investigate their possible role in fracture risk. Due to unavailable retrospective patient-specific fracture risk information, here a surrogate fracture risk based on 3D computer simulations has been employed for the statistical framework construction. When considered separately, BMD distribution performed better than shape in explaining the surrogate fracture risk variability for the analysed cohort. However, the combination of BMD and femur shape quantities in a unique statistical model yielded better results. In detail, the first shape-intensity combined mode identified using a Partial Least Square (PLS) algorithm was able to explain 70% of the surrogate fracture risk variability, thus suggesting that a more effective patients stratification can be obtained applying a shape-intensity combination approach, compared to T-score. The findings of this study strongly advocate future research on the role of a combined shape-BMD statistical framework in fracture risk determination.

Keywords – Femur fracture, Osteoporosis, Fracture risk assessment, Principal Components Analysis, Partial Least Square analysis.

INTRODUCTION

Osteoporosis is a metabolic condition which, entailing reduced bone mass and deteriorated microarchitecture, leads to increased bone fragility and, ultimately, to an increased risk of fracture [1]. In this regard, it has been reported that e.g. in the European Union 3.5 million fractures associated with osteoporosis are estimated to occur annually [2]. Osteoporotic fractures have gained progressive attention [3], owing to the increasing social and economic burden they are imposing on a rapidly ageing society [2], especially in western countries. Hip fractures, in particular, represent a major cause of mortality, disability, chronic pain and compromised quality of life [4].

Hip fractures most frequently occur after a fall in elderly people [5], a consequence of the combined reduced-with-age bone strength and of the increased probability of fall. Due to the growing global life expectancy, the incidence of hip fractures is expected to grow by 3.5 times by 2050, raising up to a total of 6.26 million [6], which emphasizes the urgent need for an accurate predictor of the risk of fracture.

Currently, the areal Bone Mineral Density (BMD) derived from Dual X-rays Absorptiometry (DXA) represents the clinical standard to assess osteoporosis status and, therefore, the fracture risk. In particular, the presence of osteoporosis is assessed using T-score (WHO report, 1994), the gold-standard derived comparing the patient-specific BMD value with the BMD value of a young, standard population. Nevertheless, the predictive performance of T-score has demonstrated to be moderate [8,9], with approximately half of the people suffering from a fracture presenting non-osteoporotic T-score levels [10]. Distilling this into practice, the BMD predictive performance suggests that although bone mass does represent an indicator, other skeletal and non-skeletal factors should markedly contribute to define the risk of fracture [8].

Computed Tomography (CT)-based Finite Element (FE) models, extensively used in osteoporosis-related research [11], would allow to reliably and comprehensively reproduce the three-dimensional patient-specific geometry and material properties, as well as load distribution. However, their cost-effectiveness has not been proved yet [12]. Moreover, CT is not routinely performed for osteoporosis diagnosis purposes, which hinders the feasibility of using CT-based models in the clinical practice.

Therefore, with the purpose of identifying clinically attainable femur geometric features, Hip Structural Analysis (HSA) [13] has been largely applied [14]. HSA-derived parameters represent proximal femur geometry attributes extracted from routine DXA images, which could be readily integrated in the clinical decision process to support T-score-based risk of fracture prediction. However, HSA-based risk prediction improvement with respect to T-score is hindered by the fact that HSA-derived parameters (1) represent discrete measures unable to describe femur shape as a whole, (2) are highly cross-correlated, and (3) are correlated with the BMD. In fact, HSA-derived parameters are extracted from the DXA bone mineral mass distribution [14] from which BMD and T-score derive as well. Moreover, HSA-derived parameters identified as the most relevant to femur fracture were not always reported to be consistent in literature [14,15].

In the last decades, statistical models as introduces by Cootes and co-workers [16] have received attention as powerful tools to investigate the morphometry of organs in relation to the diagnosis of diseases, and the bone research community has progressively realized their potential. Statistical Shape Models (SSMs) have been promisingly adopted to examine associations between the global morphometry variations in the femoral shape of an input cohort and the fracture incidence [17,18]. Similarly, the bone main BMD distribution variations have also been explored through Statistical Intensity Models (SIMs) for fracture discrimination [19–22]. In the afore-mentioned cases, the construction of the statistical models relied on Principal Component Analysis (PCA), aiming to retrospectively identify those geometric and densitometric attributes which are significantly different in fracture and non-fracture cohorts [17,18].

However, by definition PCA performs dimensionality reduction (PCA reduces the number of features by identifying the most important ones that still represent the entire dataset), but not necessarily it is optimal for classification, because it might conceal attributes which are relevant-to-fracture. In this context, Partial Least Square (PLS) algorithm [23,24] would represent a more suitable approach for the construction of statistical models aimed at diagnosis or fracture discrimination purposes, because PLS allows the extraction of the main attributes in the shape and BMD distribution which are simultaneously relevant to the fracture risk.

Taking advantage of the possibility given by a PLS-based approach, this study aims at building a modelling framework where statistical shape and intensity analysis are combined on DXA-based proximal femur geometric and densitometric data. The approach is applied to a cohort of 28 post-menopausal female subjects for whom proximal femur DXA and CT images were available. Due to the lack of information on the cohort fracture status, estimates of the Femoral Strength (FS) based on patient specific computer models [25] were used as surrogates of the subject-specific fracture risks. Therefore, the ambition is not to straightforwardly achieve a model able to improve fracture risk discrimination. Rather, the scope of the here presented work is to provide a statistical modelling framework which, employing PLS-based approaches and including both clinically available anatomical and densitometric information, could be successfully adopted in the context of fracture risk prediction, where it might also shed light on the role geometry and material properties play in relation to the fracture risk. The advantage of the here presented statistical framework is that it can be easily applied using indicators of fracture risk as obtained from a retrospective cohort.

In the following, statistical models construction is presented, together with technical remarks concerning the adopted strategies. The development of SSMs, SIMs and models gathering shape and BMD together will rely on both the standard PCA and the cutting-edge PLS approach.

MATERIALS AND METHODS

Subjects

Twenty-eight post-menopausal female subjects, aged from 55 to 81 years (70 ± 6 years) and therefore considered at increased risk of an osteoporotic fracture, were treated in San Luigi Gonzaga Hospital, Orbassano, Italy, and involved in the study after signing an informed consent. Clinical, DXA-derived data (acquired with a Discovery DXA system, Hologic) and CT scans acquired in the same year for diagnostic purposes not related to osteoporosis, were available for the whole cohort. Since the possible presence of bone metastasis might have affected bone strength, patients affected by cancer were not involved in the study.

Patient-specific surrogate marker of fracture risk

The schematic overview of the study is presented in Fig. 1. The analysed cohort does not belong to a longitudinal study, so that the fracture status of patients is undetermined because of the absence of follow-up information. To overcome this limitation, herein, a patient-specific Finite Element (FE) approach was applied to evaluate the Femoral Strength (FS) as a surrogate indicator of risk. Developed from a more comprehensive dataset than DXA-based FE models [26], femur three-dimensional CT-based FE models were used to calculate patient-specific FS values as the estimated failure loads in a sideways fall condition [25]. Technically, taking advantage of patient-specific FE models presented elsewhere [25], the impact load on the greater trochanter was linearly increased until fracture initiation, which was assessed based on principal strains failure criteria [27]. In particular here we considered fracture initiation when the number of contiguous failed cortical elements exceeded 0.3% of the total number of surface elements, as suggested elsewhere [28]. Details on FE models reconstruction and on the applied numerical settings, exhaustively reported elsewhere [25], are summarized in section 1 of the Supplementary Material. The personalized FE-based estimates of FS were employed as surrogates of hip fracture risk to be used within the performed statistical analyses (Fig. 1), aiming to identify fracture-prone morphological and densitometric attributes.

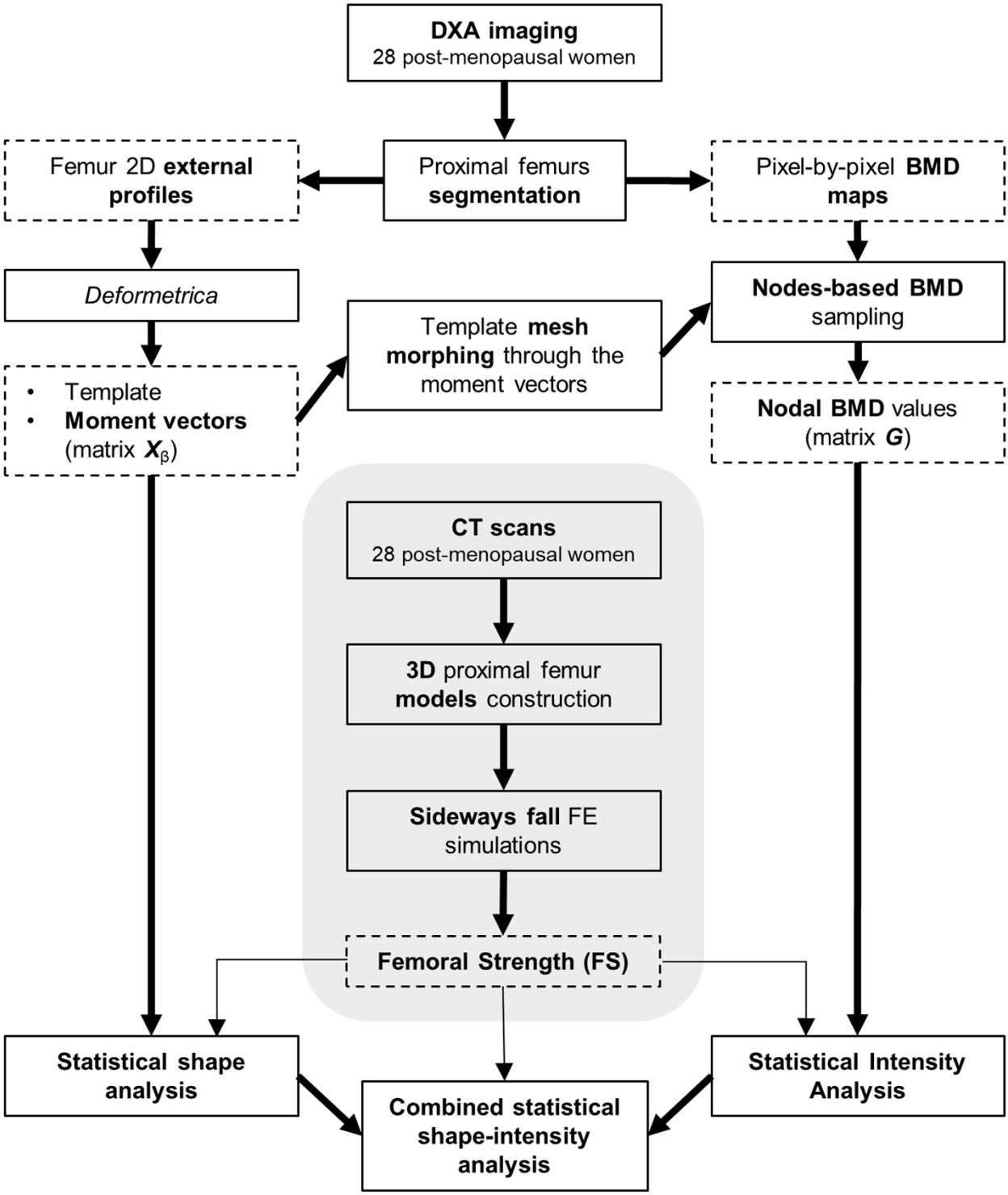

Fig. 1. Schematic overview of the workflow. Geometric information contained in DXA images was used for statistical shape analysis purposes. In particular, the software *Deformetrica* was employed to extract non-parametric shapes representations (the moment vectors), adopted as input for the SSMs construction. In addition, *Deformetrica* outputs were used in order to morph a unique mesh onto each patient-specific DXA image, so that a consistent sampling of the BMD values could be accomplished on the pixel-by-pixel BMD map extracted from the original DXA scans. The so obtained nodal BMD values were used as input for the SIMs construction. Eventually, the independent SSMs and SIMs could be unified in so called Statistical Shape-Intensity Models (SSIMs). FS values from CT-based FE analyses were used as fracture risk surrogates within the statistical analyses. The procedure to assess the surrogate fracture risk is shown with a grey background.

Statistical modelling framework

Pursuing the clinical applicability of the proposed methodologies, the whole statistical analysis involved DXA-based data: in spite of the availability of both DXA- and CT-derived proximal femur geometries and density distributions, the SSMs and SIMs were built on the two-dimensional profiles and pixel-by-pixel BMD maps extracted from DXA (Fig. 1), considering that they are currently both available in the clinical practice.

Femur Shape representation

In the here presented framework, the SSM approach relies on the mathematical framework proposed by Durrleman et al. [29], implemented in the open source code *Deformetrica* (http://www.deformetrica.org/). Contrary to the common parametric methods adopted for shape representation prior to statistical shape analysis of anatomical districts, the approach proposed in this study does not require landmarking nor point-to-point correspondence, as it relies on mathematical currents [30] to model shapes. Recalling that the current of a generic surface is defined as the flux of a test vector field across that surface, here currents act as surrogate representations of shapes and can be considered as shape indirect measures. A detailed description of the mathematical framework for shape representation is provided in section 2 of the Supplementary Material.

In this study, the input to the SSM was represented by the realigned two-dimensional DXA-derived proximal femur external shapes (Fig. S4, Supplementary Material). In detail, taking one patient as the reference, the 2D shapes were first rotated and translated so that they could be realigned with respect to the mid-point of the femur distal edge (point O in Fig. S4, Supplementary Material) and the shaft axis. After the realignment step, based on the representation of shapes via mathematical currents a generic anatomical model was provided by *Deformetrica*, which is the ensemble of (1) an average shape of the analysed cohort, the so called template $\bar{T}$, and (2) the transformation functions Φ^i mapping $\bar{T}$ to each i^{th} (*i=1….N*) patient-specific shape T^i [31,32]. Each subject-specific shape T^i can be expressed in terms of a deformed version of the template $\bar{T}$, and of a term ε^i, accounting for features not captured by the deformed template, according to:

$$T^i = \Phi^i \cdot \bar{T} + \varepsilon^i \qquad (1)$$

The template deformation function Φ^i is driven by a set of moment vectors $\boldsymbol{\beta}^i$ centred at a grid of control points which are defined with respect to the template $\bar{T}$, and which encompass the morphological attributes of the i^{th} patient-specific shape (Fig. 2a).

Before presenting the detailed SSMs and SIMs construction, technical remarks pertaining the two strategies adopted for developing the statistical models are provided.

Remarks on statistical modelling

SSMs and SIMs are modelling strategies based on the identification of (1) an average shape (in our case, femur shape) or intensity (in our case, the pixel-by-pixel BMD map), representing those shape features common to cohort under study, and (2) the main modes of variation from the average shape. Roughly, the idea at the basis of the statistical modelling is that by selecting a limited number of modes, the shape or the intensity distribution of any individual belonging to a specific population can be adequately described. In this study, two different approaches were implemented to build statistical shape and intensity models of the analysed femurs cohort, the Principal Component Analysis (PCA) and the Partial Least Square (PLS) analysis.

Principal Components Analysis

PCA, an exploratory multivariate statistical technique for simplifying complex datasets, was applied to extract the main shape and BMD distribution attributes from the cohort under study. Technically, given *N* observations on *k* variables, the PCA goal consists in reducing the dimensionality of the input data matrix by finding *m* new variables (with $m < k-1$), termed principal components, which together account for as much as possible of the variance in the original *k* variables while remaining mutually uncorrelated and orthogonal [33]. After identifying the directions, called principal modes, which maximise the variance of the original variables, the principal components are found by projecting the original *k* variables onto the principal modes. Here, each principal component discloses the mode contribution to the subject-specific femur shape or intensity. PCA theory and related mathematics are extensively detailed in section 3 of the Supplementary Material.

Partial Least Square Analysis

Analogous to PCA, PLS performs dimensionality reduction, and here was applied to identify the main shape and BMD distribution attributes simultaneously relevant to the surrogate fracture risk. Given an input data matrix *X* and a response variable *Y*, PLS computes the directions in the space of the variables, termed PLS modes, where the covariance between *X* and *Y* is maximal. By projection of the original data matrix *X* onto the PLS modes, the PLS components are identified which best account for the variance of *X*, *Y* and the correlation between the two. Taking the surrogate fracture risk as the response variable, PLS allowed to identify the main shape and BMD distribution attributes simultaneously relevant to the surrogate fracture risk too.

PLS theory and its implementation are extensively detailed in section 4 of the Supplementary Material.

Statistical Shape Model

The statistical shape analysis was built up on patient-specific moment vectors $\boldsymbol{\beta}^i$, encompassing the proximal femur anatomical attributes of the i^{th} subject (Fig. 1). Prior to the SSMs construction, vectors $\boldsymbol{\beta}^i$ were used to build up the moment vectors matrix $\boldsymbol{X}_\beta$ (Fig. 2a), on which PCA and PLS were implemented. PCA was performed to identify the main geometrical attributes observed in the cohort, and allowed the extraction of the deformation modes together with their respective variance [16] and corresponding shape principal components. Determined as projection of the original moment vectors matrix on the i^{th} PCA mode, principal components here describe the extent of the deformation the template undergoes along the i^{th} direction to match each subject's shape. The principal components give therefore a quantitative representation of the subject-specific shape attributes encompassed in each mode.

Subsequently, in order to identify fracture-prone proximal femur morphological attributes, PLS was applied to the moment vectors matrix $\boldsymbol{X}_\beta$, taking the centred FS vector ($\mathrm{FS} = \mathrm{FS}^{original} - \overline{\mathrm{FS}}$) as the response variable. The PLS shape modes were identified, automatically ordered by decreasing variance and correlation with respect to the response variable. Analogous to PCA, the i^{th} PLS components delineate the i^{th} PLS mode contribution to the patient-specific shape.

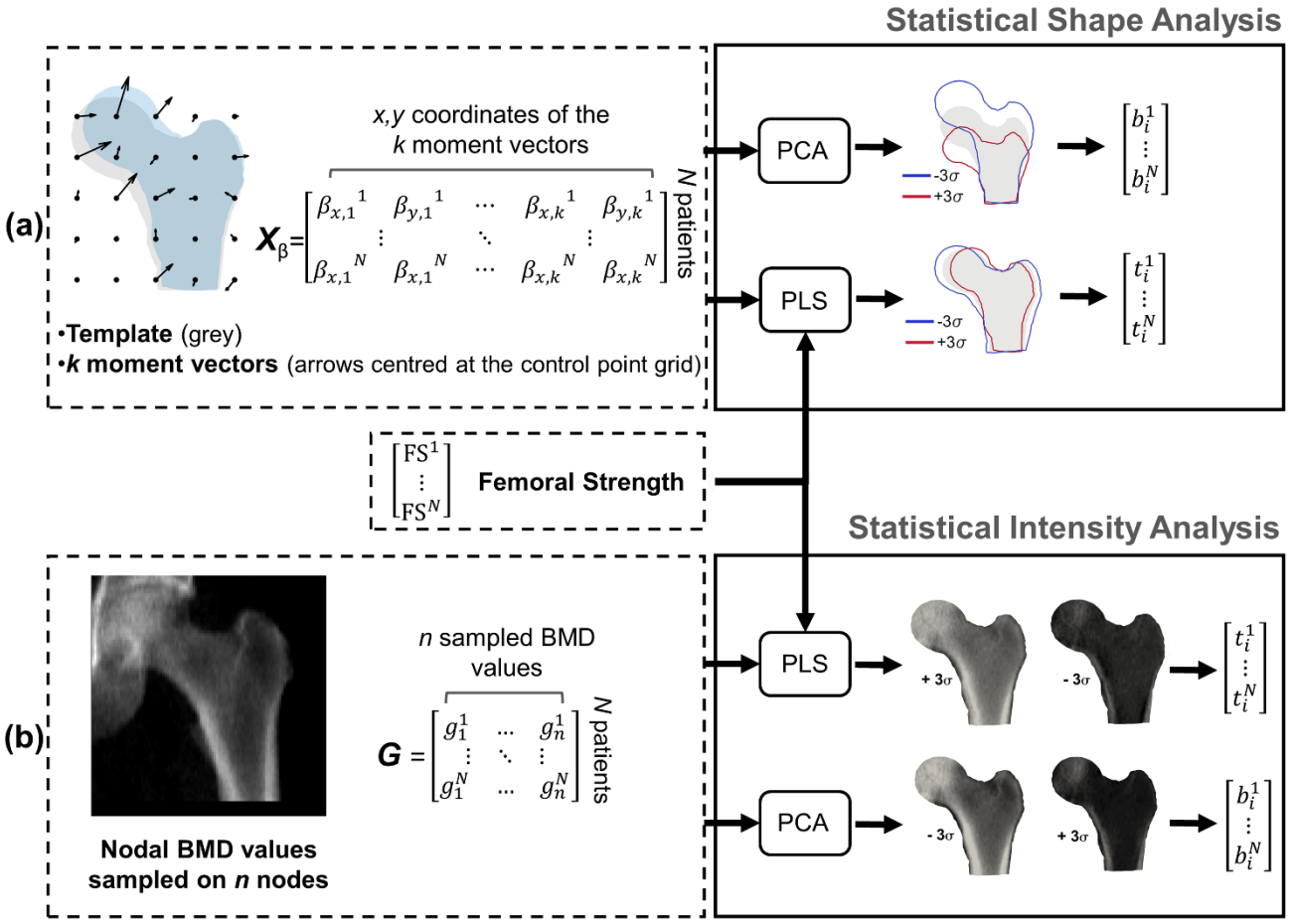

Fig. 2. Statistical analysis pipeline. As delineated in the lower portion of Fig. 1, the statistical shape and intensity analyses, here illustrated in greater detail, were based on the patient-specific moment vectors and nodal BMD values respectively. (a) **Statistical Shape Analysis**. The SSMs were developed using the *N* x 2*k* moment vectors matrix x_β as input, with *N* being the total number of patients and *k* dependent on the number of control points. With PCA, the main deformation modes were identified, while with PLS, which took the FS array as an additional input too, the main deformation modes relevant to the FS were found. By projecting the original data matrix on the identified modes, the principal (***b***$_i$) and PLS (***t***$_i$) shape components for each i^{th} mode (*i = 1,…N-1*) could be computed. (b) **Statistical Intensity Analysis**. The SIMs were developed using the *N* x *n* BMD matrix ***G***, with *N* the total number of patients and *n* the number of mesh nodes on which the BMD was extracted. With PCA, the main intensity modes were identified, while with PLS, which took the FS array as an additional input, the main intensity modes relevant to the FS were found. By projecting the original data matrix on the identified modes, the principal (***b***$_i$) and PLS (***t***$_i$) intensity components for each i^{th} mode (*i* = 1,…N-1) could be computed.

Statistical Intensity Model

Despite providing information regarding the shape, the SSM approach does not account for the density distribution within bones, the other crucial determinant of bone strength. To overcome this limitation, here a SIM approach is proposed, which requires local density information as well as a consistent spatial correspondence of the locations where the BMD is sampled in input patients. With

this aim, recalling Eq. 1, moment vectors $\boldsymbol{\beta}$ were used to morph the meshed template (1 mm size triangular elements) towards each patient (Fig. 1). More in detail, moment vectors $\boldsymbol{\beta}$ were used to morph a unique mesh onto each patient-specific DXA, so that the BMD value associated to each image pixel was assigned to the corresponding node located in the pixel. Therefore, BMD values were consistently sampled over the DXA images, and subsequently gathered in arrays $\boldsymbol{g}$. The patient-specific BMD arrays $\boldsymbol{g}$ were organized in a $N \times n$ matrix $\boldsymbol{G}$ (Fig. 2b), N being the number of observations (i.e. the patients), and n the number of variables, i.e. the total number of nodes. No density values normalization procedure [18] was performed, since the intensity values were actually BMD values instead of grey values.

After centring the matrix with respect to the average BMD values array, PCA was performed on the matrix $\boldsymbol{G}$ according to the method described elsewhere [16]. PCA intensity modes and their corresponding variance were obtained, together with the principal intensity components, describing the contribution of each principal mode of variation of BMD to the patient-specific i^{th} BMD distribution.

Subsequently, PLS was performed on the patient-specific BMD vectors matrix $\boldsymbol{G}$ taking the FS as the response variable, aiming to assess the BMD distribution attributes mostly related to the surrogate fracture risk. Hence, PLS intensity modes and the corresponding intensity PLS components (Fig. 2b) were identified.

Combined Statistical Shape-Intensity Model

With the purpose of unifying the previously presented independent statistical shape and intensity models, to make the representation more compact and complete, a so called Statistical Shape-Intensity Model (SSIM) [34] was built. This allowed to account for the shape and density distribution together. The procedure is based on the application of PCA and PLS on PCA- and PLS-based outcomes previously obtained considering shape and intensity features separately (Fig. 1).

In the case of PCA, the shape and intensity principal components were gathered in two matrices $\boldsymbol{B}^S$ and $\boldsymbol{B}^G$, respectively, containing the principal components as columns (Fig. 2a). The two matrices $\boldsymbol{B}^S$ and $\boldsymbol{B}^G$ were concatenated into the matrix $\boldsymbol{B}$:

$$\boldsymbol{B} = \begin{pmatrix} \boldsymbol{W}_{PCA}\boldsymbol{B}^{S} \\ \boldsymbol{B}^{G} \end{pmatrix} = \begin{pmatrix} \boldsymbol{W}_{PCA}\boldsymbol{\Phi}^{S'}\boldsymbol{X}'_{\beta} \\ \boldsymbol{\Phi}^{G'}\boldsymbol{G}' \end{pmatrix}. \qquad (2)$$

where $\boldsymbol{W}_{PCA}$ is a weighting factor matrix, expressed as:

$$\boldsymbol{W}_{PCA} = r\,\boldsymbol{I}, \qquad (3)$$

where r is the ratio between the total variance in only intensity and the total variance in only shape PCA modes [34], and $\boldsymbol{I}$ is the identity matrix. The matrices $\boldsymbol{\Phi}^{S}$ and $\boldsymbol{\Phi}^{G}$ gather the only shape and only intensity modes, respectively, as previously extracted. By applying PCA onto the concatenated matrix $\boldsymbol{B}$, combined shape-intensity PCA modes were identified. Subsequently, by projection of the matrix $\boldsymbol{B}$ onto the identified PCA subspace, the patient-specific combined shape-intensity principal components were obtained.

Analogously, in the PLS case, a concatenated shape and intensity PLS components matrix $\boldsymbol{T}$ was built up, based upon the only shape and only intensity PLS components previously computed as follows:

$$\boldsymbol{T} = \begin{pmatrix} \boldsymbol{W}_{PLS}\,\mathbf{P}^{S'}\boldsymbol{X}'_{\beta} \\ \mathbf{P}^{G'}\boldsymbol{G}' \end{pmatrix}, \qquad (4)$$

where $\boldsymbol{W}_{PLS}$ is the weighting factor matrix with the same expression as $\boldsymbol{W}_{PCA}$, but declined to PLS, and $\mathbf{P}^{S}$ and $\mathbf{P}^{G}$ the matrices containing the only shape and only intensity PLS modes as previously identified. By applying PLS onto the concatenated matrix $\boldsymbol{T}$, combined shape-intensity PLS modes were identified. Subsequently, by projection of the matrix $\boldsymbol{T}$ onto the identified PLS subspace, the patient-specific combined shape-intensity PLS components were obtained.

RESULTS

Statistical Shape Model

A total number of 25 moment vectors $\boldsymbol{\beta}$ ($\boldsymbol{x}, \boldsymbol{y}$ pairs) per patient were obtained, and a 27×50 moment vectors matrix $\boldsymbol{X}_{\beta}$ was built. One of the patients was indeed excluded from the whole statistical modelling since the shape reconstruction error was 4 times higher than the average error.

The first 7 PCA modes, able to explain almost the entire shape variance, can be visualized in Fig. S7 of the Supplementary Material. Mode 1, which embodies the most variable features within the considered cohort, can be related to the size. In addition, mode 1 and mode 2, are significantly correlated with the Hip Axis Length (HAL) (Table 1), thus suggesting that HAL is a highly variable feature in the observed cohort, the first two modes together gathering the 80% of the total shape variance. Interestingly, none of the 7 PCA modes was found to be correlated with the FS. The herein mentioned HSA-related parameters and regions are graphically displayed in Fig. S6 of the Supplementary Material.

Table 1. Main significant correlations found between the SSMs modes and DXA-related parameters.
HAL: Hip Axis length; NSA: Neck-Shaft Angle; nn: narrow-neck; it: intertrochanter.

SSM: PCA			**SSM: PLS**		
Variable	R	*p*	Variable	R	*p*
mode1			**mode 3**		
HAL	-0.54	0.0035	**HAL**	0.48	0.0107
mode 2			**NSA**	-0.56	0.0026
HAL	0.66	0.0002	**nn Width**	0.45	0.02
it Width	0.42	0.0305	**it Width**	0.47	0.01
			FS	0.36	0.049

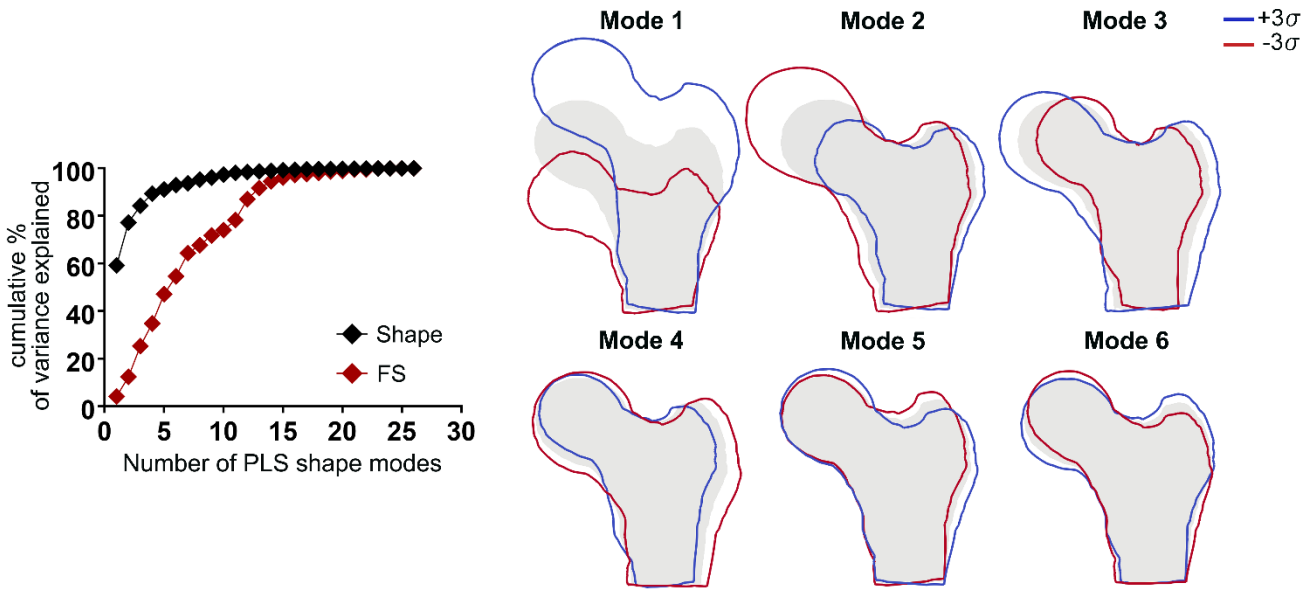

Fig. 3. The cumulative percentage of variance explained by the PLS modes (left) and the first 6 PLS shape modes shown as deformations of the template along each mode between $-3\sqrt{\sigma^2}, 3\sqrt{\sigma^2}$, σ^2 being the m^{th} PLS mode variance (right). The first 6 modes disclose 93% of the shape and 54.6% of the FS variance. By construction, each mode moves towards $+3\sigma$ when the FS increases. Hence, the -3σ deformation mode is here evidence of an increased risk of fracture. On the whole, 11 modes describe 98.16% of the variability in shape and 78.27% of the variability in the FS. In order to achieve 95% of the FS variability explained through shape-based modes, 15 modes are necessary (explaining 99.2% of the shape variance).

With a deep interest in the anatomical features most meaningful to the surrogate fracture risk, PLS was performed employing the FS risk indicator as the external response variable. It emerged that a total of 11 PLS modes explain at least 75% of the variance observed in the FS (Fig. 3). Fig. 3 presents the first 6 PLS modes. It can be noticed that although mode 1 explains most of the shape variance, the mode explaining the majority of the variability in the FS is mode 3 (Table 1), which combines alterations in the intertrochanter and neck width, as well as in the length and inclination of the neck, as witnessed by the identified significant correlations with the related HSA-derived parameters (Table 1). The analysis of PLS shape mode 3 *vs.* FS risk predictor is presented in Fig. 4a. In conjunction with the inconsistently explained shape and FS variability by the first PLS shape modes shown in Fig. 3, it may advocate a limited role of the femur shape in explaining the variations observed in the FS.

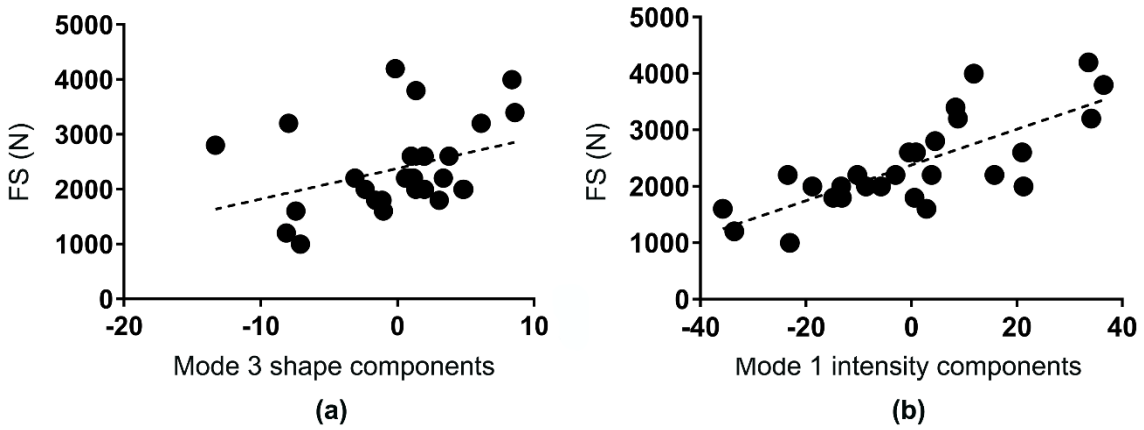

Fig. 4. The PLS components stratification performances. (a) The third PLS shape component *vs.* the FS (R = 0.36, $p = 0.049$); (b) the first PLS intensity component *vs.* FS risk predictor. (R = 0.76, $p < 0.0001$).

Statistical Intensity Model

A total of 21 PCA modes were necessary to explain at least 95% of the density distribution variability (Fig. S8), and the first 8 PCA intensity modes are displayed in Fig. S8 of the Supplementary Material. The first PCA intensity mode, which highlights an overall variation in the BMD within the whole proximal femur, was (as expected) significantly correlated with the T-score (total femur) and BMD, but also with Buckling-Ratio and Cross-Sectional Moment of Inertia [13,35], confirming the tight link of these quantities with the intensity distribution on which their computation relies on (Table 2). At the same time, the first PCA intensity mode was also inversely correlated with FS (Table 2), suggesting that the material properties of the femur may play a crucial role in the context of a fracture. PCA intensity mode 2 highlights a decreased BMD in the trochanteric fossa region, which also comes with a thicker cortex layer medially in the femur distal portion (Fig. S8, Supplementary Material). Similarly, PCA intensity mode 3 is representative of a decreased BMD area in the greater trochanter region. Interestingly, PCA intensity modes 2 and 3 were both correlated with HAL (Table 2).

As far as the PLS intensity modes are concerned, the first 4 modes, displayed in Fig. 5, describe 97.71% of the FS variability, but only 51.71% of the intensity variability. Interestingly, the PLS first intensity modes turned out to be very similar to the corresponding PCA ones, highlighting again, beyond the variability in the distribution of BMD as a whole, the variations at the intertrochanteric fossa and greater trochanter. In analogy with the PCA intensity modes obtained outcome, the PLS intensity mode 1 was markedly correlated with BMD, with the BMD distribution-based HSA-derived parameters (e.g.

T-score, narrow-neck BMD, narrow-neck Buckling-Ratio, intertrochanteric BMD), as well as with FS (Table 2, see also Fig. 4b). Furthermore, also the PLS intensity mode 2 resulted significantly correlated with FS, while an association emerged between PLS intensity mode 4 and HAL (Table 2). In Fig. 4b PLS intensity mode 1 *vs.* FS risk predictor is presented, which points out PLS intensity mode 1 superior role with respect to PLS shape mode 3.

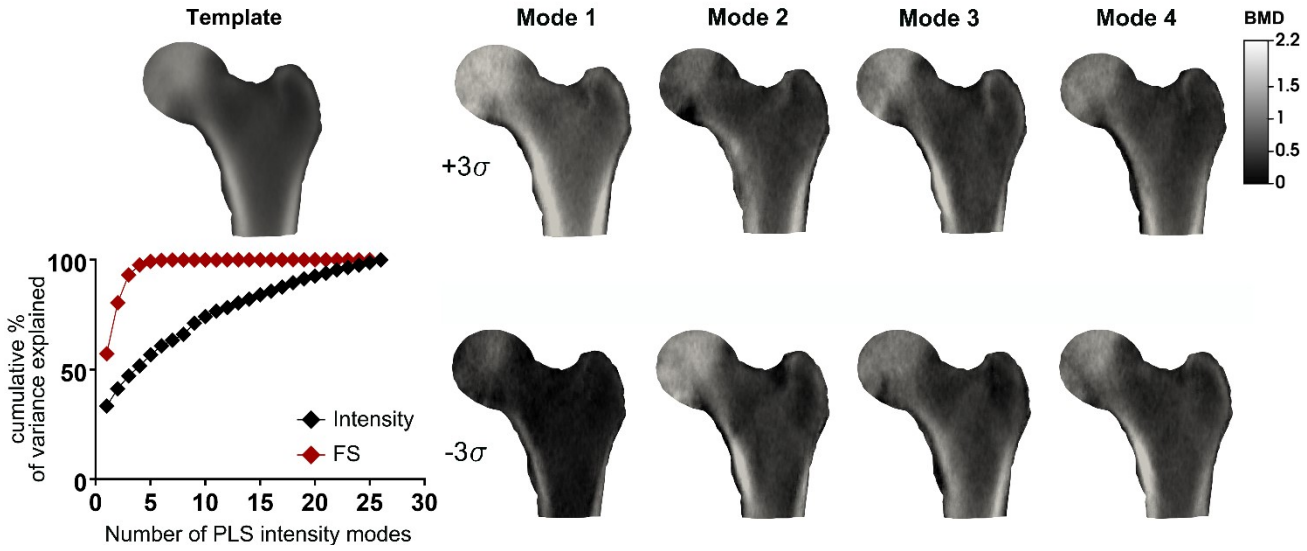

Fig. 5. Visualization of the first 4 PLS intensity modes. For each mode, the BMD distribution is determined letting the average BMD distribution vary between $-3\sqrt{\sigma^2}, 3\sqrt{\sigma^2}$, σ^2 referring to the PLS intensity mode variance. The -3σ direction, associated to a decreased strength, is that at higher risk. BMD is expressed in g/cm^2. The cumulative percentage of variance explained by the PLS intensity modes is also shown in the bottom-right side.

Table 2. Main significant correlations found between the SIMs modes and DXA-related parameters.
BR: Buckling Ratio; CSMI: Cross-Sectional Moment of Inertia; HAL: Hip Axis length; nn: narrow-neck; it: intertrochanter.

SIM: PCA			**SIM: PLS**		
Variable	R	*p*	Variable	R	*P*
mode 1			**mode 1**		
T-score	−0.90	< 0.0001	**T-score**	0.92	< 0.0001
BMD	−0.94	< 0.0001	**BMD**	0.95	< 0.0001
nn BMD	−0.93	< 0.0001	**nn BMD**	0.93	< 0.0001

it BMD	-0.82	< 0.0001	**it BMD**	0.8	< 0.0001
nn BR	0.78	< 0.0001	**nn BR**	−0.78	< 0.0001
it BR	0.75	< 0.0001	**it BR**	−0.78	<0.0001
nn CSMI	−0.55	0.0027	**nn CSMI**	0.56	0.0026
it CSMI	−0.48	0.011	**it CSMI**	0.45	0.0184
FS	−0.69	< 0.0001	**FS**	0.76	< 0.0001
mode 2			**mode 2**		
HAL	0.42	0.032	**FS**	0.48	0.01
mode 3			**mode 4**		
HAL	−0.61	< 0.001	**HAL**	−0.46	0.02

Combined Statistical Shape-Intensity Model

A total of 18 PCA SSIM modes explained the 95% of the combined intensity and shape variance, the first 6 of them accounting for the 75% of it (Fig. S9 of the Supplementary Material). Among them, only the second PCA SSIM mode was significantly correlated to FS. Analogous to the first PCA intensity mode, the second PCA SSIM mode carried the majority of the intensity-related information, strongly correlated to the T-score and BMD (Table 3).

As for the PLS-based analysis the first three PLS SSIM modes explained 96.72% of FS variance and 56.75% of the combined intensity and shape variability (Fig. 6), with the first two PLS SSIM modes accounting for the 83% of the FS variance. It emerged from the analysis that the first two PLS SSIM modes were both significantly correlated with the FS (Table 3).

Table 3. Main significant correlations found between the SSIMs modes and DXA-related parameters.
HAL: Hip Axis length; BR: Buckling Ratio; CSMI: Cross-Sectional Moment of Inertia; nn: narrow-neck; it: intertrochanter.

SSIM: PCA			SSIM: PLS		
Variable	R	*p*	Variable	R	*P*
mode 1			**mode 1**		
HAL	-0.51	0.0061	**T-score**	0.84	< 0.0001
mode 2			**BMD**	0.84	< 0.0001
T-score	0.86	< 0.0001	**nn BMD**	0.79	< 0.0001
BMD	0.92	< 0.0001	**it BMD**	0.61	< 0.001
nn BMD	0.93	< 0.0001	**nn BR**	-0.62	< 0.001
it BMD	0.81	< 0.0001	**it BR**	-0.66	< 0.0002
nn BR	-0.78	< 0.0001	**nn CSMI**	0.58	0.0016
it BR	-0.75	< 0.0001	**FS**	0.82	< 0.0001
nn CSMI	0.52	0.0054	**mode 2**		
it CSMI	0.44	0.0215	**it BMD**	0.47	0.0128
FS	0.66	< 0.0002	**nn BR**	-0.40	0.0372
			FS	0.40	0.037

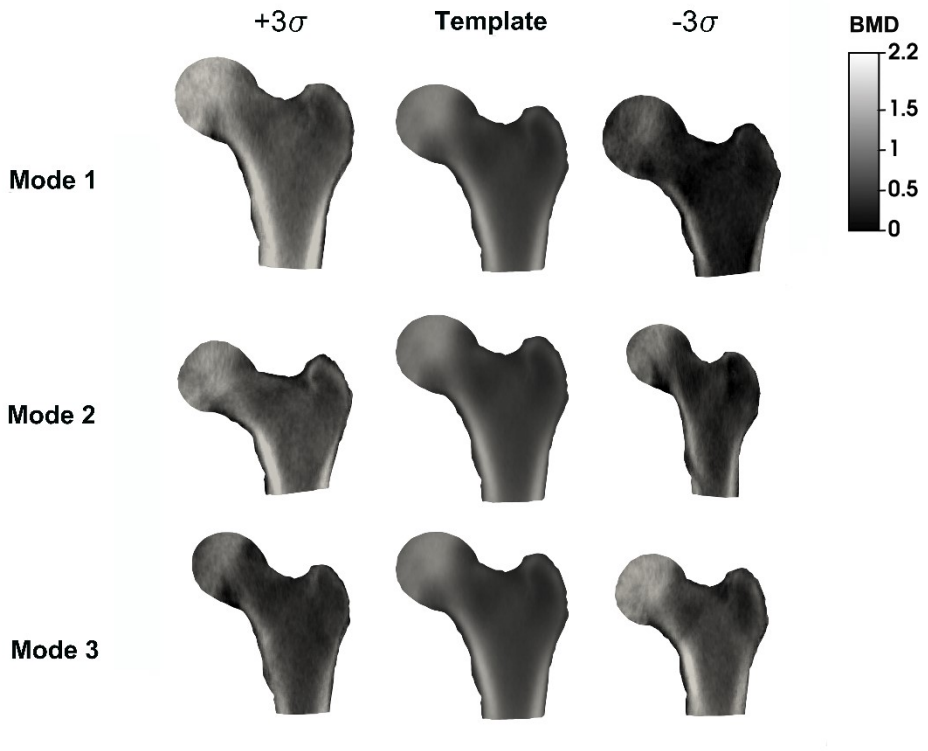

Fig. 6. The first 3 combined shape-intensity PLS modes. The -3σ direction, associated to a decreased strength, is that at higher risk. σ refers to each mode standard deviation. BMD is expressed in g/cm^2.

The PLS SSIM first components *vs.* FS are depicted in Fig. 7a, while Fig. 7b presents the PLS SSIM first components *vs.* T-score. By projecting the patient-specific moment vectors and BMD values on the previously identified first PLS combined mode, the shape-intensity components of two additional patients who had fractured in the same year of their DXA could be computed and are displayed as empty circles. Notably, a good stratification is achieved for the osteopenic patients, with the two fractured patients located in the higher risk region (the lower the first SSIM components, the lower the FS and therefore the higher the risk of fracture, see Fig. 7a). Beyond the fractured patient, also other osteopenic patients would be judged at an increased risk of fracture.

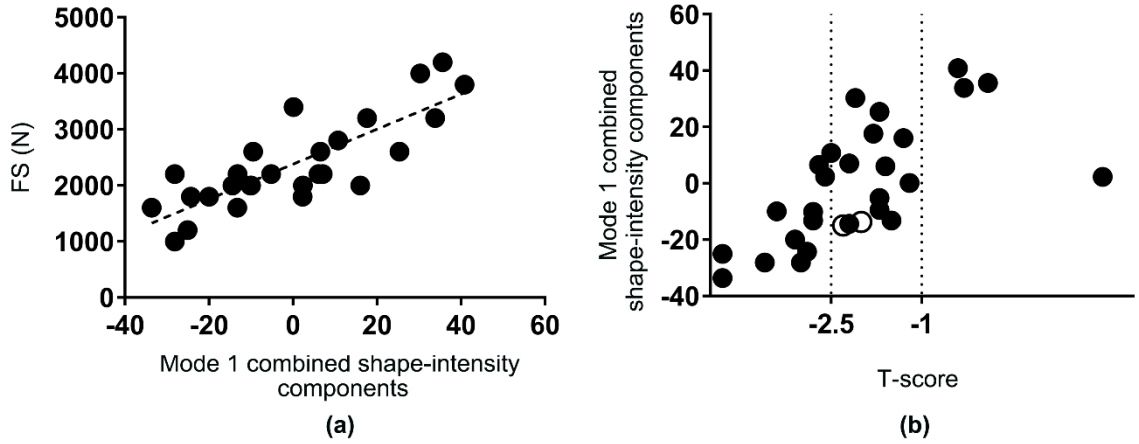

Fig. 7. The PLS combined components stratification performances. **(a)** the first mode combined shape-intensity components *vs* the FS ($R = 0.82$, $p < 0.0001$). In all these cases, decreasing the weighting term of the respective modes, the FS decreases and thus the surrogate fracture risk increases. **(b)** Comparison between the first PLS combined shape-intensity mode shape components and T-score classification performances. The two fractured patients, whose shape-intensity components have been determined *a posteriori* based on the previously determined PLS space, are represented with empty circles.

DISCUSSION

In this study, a statistical modelling framework based on proximal femur geometric and densitometric data as obtained from DXA is presented. The main aim of this study was to test the effectiveness of a combined statistical framework (1) for the assessment of the hip risk of fracture, fostering its adoption in the context of the proximal femur fracture risk prediction, and (2) more in general, for investigating the role that geometry and BMD play in determining proximal femur fracture.

The rationale at the basis of the proposed combined statistical approach is in the fact that: (1) in contrast to the discrete and cross-correlated geometric attributes representation given by the HSA-derived parameters, statistical shape modelling allows to capture the global geometric heterogeneity in the cohort; (2) geometry attributes and intensity features dependence on bone tissue adaptation process [36] prompts the need to account for them together.

Technically, the application of PCA highlighted the anatomical attributes and densitometric features disclosing most of the variability in the cohort. When accounting for the main anatomical attributes alone, no significant links to the FS emerged. This is consistent with the fact that PCA, *per se*, can

identify features suitable for representing information, though not necessarily optimal for classification purposes. From this perspective, when only the intensity distribution was considered, the first PCA mode turned out to be negatively correlated with FS ($R = -0.69$, $p < 0.0001$), pointing out a significant link between BMD distribution and the surrogate marker of fracture risk, ultimately suggesting that density might be able to explain the majority of the surrogate fracture risk variance. Moreover, the considerable number of PCA intensity modes necessary to disclose most of the intensity variability (21 PCA modes explain 95% of the BMD distribution variability) suggests more complex inter-variability patterns in the BMD distribution, compared to geometry.

In this light, unifying shape and intensity in a combined PCA-based SSIM, the combined mode 2 emerged as strongly associated with BMD variability (corroborated by its strong correlation with the T-score and BMD, as shown in Table 3), and explained most of the FS variability. The first PCA-based combined mode highlighted mainly the variability in femur shape, while carrying much less BMD variation. Nonetheless, in spite of the prevalent BMD role, the PCA-based combined second mode also encompassed changes in the femoral neck angle, width and length (Fig. S9). These findings agree with previous studies accomplished developing statistical shape and intensity individual modes in a retrospective cohort [21].

The dimensionality reduction obtained applying a PLS-based strategy highlighted that shape modes alone were moderately effective in explaining FS variability: the PLS-based shape first mode, alone able to describe more the 50% of the total shape variance, covered only a very small percentage of the FS variability (4.12%, Fig. 3); a total of 6 PLS-based shape modes, capturing more than 90% of the shape variance, were required to achieve a 50% explanation of FS variance. The PLS-based shape third mode was the one explaining the largest portion of FS variance (13%) combining, from a morphological perspective, variability in the neck inclination and length with variability in the intertrochanteric and shaft width.

Focusing on PLS-based intensity analysis, shown in Fig. 5, a situation which appears reversed if compared to the PLS-based shape analysis is visible: only a few modes, although able to disclose only about 50% of the BMD distribution variability, explain a considerable percentage of the FS variability

(the first 4 modes explain 97.71% of the FS variability, but only 51.71% of the intensity variability). This appears as evidence of a pivotal role played by the material properties against the FS, suggesting a secondary role for the shape. It is therefore not surprising that the main PLS-based intensity modes appear markedly similar to PCA-based ones (given that the intensity variability in itself was already tightly related to that of the FS).

The PLS-based combined model yielded interesting results. First of all, the PLS-based combined shape-intensity modes were effective in the stratification of the patients within the three T-score categories (osteoporosis: T-score<−2.5; osteopenia: −2.5<T-score<−1; non-osteoporosis: T-score>−1), with the two fractured osteopenic patients reasonably located at high risk (Fig. 7b). On top of that, the combination of shape and intensity yielded an improvement in the proportion of FS variance explained with respect to the intensity alone. Looking at Fig. 7a indeed, the improved shape-intensity relation with the FS is visible: the first PLS-based intensity mode explained 57.18% of the FS variability (Fig. 4b), unquestionably better than the third shape mode (Fig. 4a). Nevertheless, the first PLS-based shape-intensity mode explained the 66.9% of FS variability (Fig. 7a). Although intensity appeared predominant in explaining most of the estimated FS and correlated to the most meaningful shape features, the inclusion of the PLS deformation modes still led to a marked improvement in risk prediction.

This study presents limitations that may weaken the current findings. A possible limitation could be represented by the limited number of patients involved in the study. Dealing with the construction of statistical models, we acknowledge that the outcome of this study would have undoubtedly benefited from a larger cohort, which might have disclosed features here not accounted for. Moreover, the effectiveness of combined statistical model was tested adopting a surrogate indicator of the risk of fracture, FS, obtained from patient-specific FE simulations. This choice was dictated by the lack of follow up in the analysed cohort. In spite of the enclosed uncertainty associated with this judgement call, the use made of FS allowed to relatively estimate a patient-specific risk level and thus to obtain, from a relative intra-cohort perspective, reasonable results. Finally, it must be recalled that using PLS as a basis of representation does not necessarily assures orthogonality, and therefore independence

of modes. However, using the combined statistical framework based on PLS has allowed a further compression of the basis of representation, allowing shape-intensity similarities and differences to emerge in the dataset. This is confirmed by the fact that the combined PLS-based statistical framework ultimately focused on one only mode.

Despite the afore-mentioned limitations, the herein presented combined statistical modelling approach appears extremely encouraging from the perspective of the assessment of the risk of fracture of the proximal femur. Once the PLS-based combined shape-intensity space is built based on a training set, any new patient could be simply projected on this space in order to assess the patient-specific shape-intensity component, one unique number per mode gathering shape and BMD information together. Interestingly, the information required by this procedure would be currently attainable in the clinical practice. This would require, of course, a larger training set. As repeatedly claimed, the statistical framework is here built with reference to a surrogate marker of fracture risk, lacking retrospective information about the analysed cohort. However, the illustrated procedure has proved promising and attractive, with the potential to accomplish diagnostic improvement, and could be easily adopted on a larger cohort with available fracture status information.

In conclusion, despite other studies have explored the use of DXA-based statistical shape and intensity models retrospectively, aiming to achieve through the adoption of PCA an improved osteoporotic fracture risk prediction [21,37,38], the interaction and inter-dependency between shape and density rarely investigated. Here, a combined shape-intensity PLS-based statistical model has demonstrated its potential in assessing the hip fracture risk, with findings supporting the hypothesis that the interplay between shape and BMD distribution should be explored more in depth, given the profound and complex interrelation existing between the shape and the BMD distribution in a living and continuously loaded tissue [36].

COMPLIANCE WITH ETHICAL STANDARDS

Conflict of Interest The authors of this article declare no potential conflicts of interest.

Informed Consent The authors of this article declare that informed consent was obtained from all the patients involved in the study.

DECLARATIONS

Funding This research received no external funding.

Availability of data and material The datasets generated during the current study are available from the corresponding author on reasonable request.

Authors' contributions All authors have contributed to the conception and design of the study, the interpretation of data, and the drafting of the article. Alessandra Aldieri and Mara Terzini post-processed the medical images and worked on the statistical models construction. Cristina Bignardi supervised the images collection as well as their processing for the FE construction. Alberto L. Audenino gave hints and advice for the FE modelling and the statistical framework outcomes interpretations. Umberto Morbiducci supervised the whole work and its objectives, especially in the context of the statistical modelling procedures.

ACKNOWLEDGMENTS

The authors would like to thank Giangiacomo Osella from San Luigi Gonzaga Hospital, Orbassano, for the DXA and CT images collection and Margaret Paggiosi, from the Department of Oncology and Metabolism, University of Sheffield, for kindly providing the pixel-by-pixel BMD maps.

REFERENCES

[1] Consensus development conference: Diagnosis, prophylaxis, and treatment of osteoporosis, Am. J. Med. 94 (1993) 646–650. https://doi.org/10.1016/0002-9343(93)90218-E.

[2] J.A. Kanis, C. Cooper, R. Rizzoli, J.-Y. Reginster, European guidance for the diagnosis and management of osteoporosis in postmenopausal women, Osteoporos. Int. 30 (2019) 3–44. https://doi.org/10.1007/s00198-018-4704-5.

[3] O. Ström, F. Borgström, J.A. Kanis, J. Compston, C. Cooper, E. V. McCloskey, B. Jönsson,

Osteoporosis: burden, health care provision and opportunities in the EU, Arch. Osteoporos. 6 (2011) 59–155. https://doi.org/10.1007/s11657-011-0060-1.

[4] L.J. Melton, III, T.M. Therneau, D.R. Larson, Long-Term Trends in Hip Fracture Prevalence: The Influence of Hip Fracture Incidence and Survival, Osteoporos. Int. 8 (1998) 68–74. https://doi.org/10.1007/s001980050050.

[5] J. Parkkari, P. Kannus, M. Palvanen, A. Natri, J. Vainio, H. Aho, I. Vuori, M. Järvinen, Majority of Hip Fractures Occur as a Result of a Fall and Impact on the Greater Trochanter of the Femur: A Prospective Controlled Hip Fracture Study with 206 Consecutive Patients, Calcif. Tissue Int. 65 (1999) 183–187. https://doi.org/10.1007/s002239900679.

[6] N. Harvey, E. Dennison, C. Cooper, Osteoporosis: impact on health and economics, Nat. Rev. Rheumatol. 6 (2010) 99–105. https://doi.org/10.1038/nrrheum.2009.260.

[7] Assessment of fracture risk and its application to screening for postmenopausal osteoporosis. Report of a WHO Study Group., World Health Organ. Tech. Rep. Ser. 843 (1994) 1–129. http://www.ncbi.nlm.nih.gov/pubmed/7941614.

[8] J.A. Kanis, E. V. McCloskey, H. Johansson, A. Oden, Approaches to the targeting of treatment for osteoporosis, Nat. Rev. Rheumatol. 5 (2009) 425–431. https://doi.org/10.1038/nrrheum.2009.139.

[9] S.A. Wainwright, L.M. Marshall, K.E. Ensrud, J.A. Cauley, D.M. Black, T.A. Hillier, M.C. Hochberg, M.T. Vogt, E.S. Orwoll, Hip Fracture in Women without Osteoporosis, J. Clin. Endocrinol. Metab. 90 (2005) 2787–2793. https://doi.org/10.1210/jc.2004-1568.

[10] S. Baim, W.D. Leslie, Assessment of Fracture Risk, Curr. Osteoporos. Rep. 10 (2012) 28–41. https://doi.org/10.1007/s11914-011-0093-9.

[11] M.L. Bouxsein, P. Zysset, C.C. Glüer, M. McClung, E. Biver, D.D. Pierroz, S.L. Ferrari, Perspectives on the non-invasive evaluation of femoral strength in the assessment of hip fracture risk, Osteoporos. Int. (2020). https://doi.org/10.1007/s00198-019-05195-0.

[12] M. Viceconti, M. Qasim, P. Bhattacharya, X. Li, Are CT-Based Finite Element Model Predictions of Femoral Bone Strengthening Clinically Useful?, Curr. Osteoporos. Rep. 16 (2018) 216–223. https://doi.org/10.1007/s11914-018-0438-8.

[13] T.J. Beck, Extending DXA beyond bone mineral density: Understanding hip structure analysis, Curr. Osteoporos. Rep. 5 (2007) 49–55. https://doi.org/10.1007/s11914-007-0002-4.

[14] J.S. Gregory, R.M. Aspden, Femoral geometry as a risk factor for osteoporotic hip fracture in men and women, Med. Eng. Phys. 30 (2008) 1275–1286. https://doi.org/10.1016/j.medengphy.2008.09.002.

[15] V.E. Dinçel, M. Şengelen, V. Sepici, T. Çavuşoğlu, B. Sepici, The association of proximal femur geometry with hip fracture risk, Clin. Anat. 21 (2008) 575–580. https://doi.org/10.1002/ca.20680.

[16] T.F. Cootes, C.J. Taylor, D.H. Cooper, J. Graham, Active Shape Models-Their Training and Application, Comput. Vis. Image Underst. 61 (1995) 38–59. https://doi.org/10.1006/cviu.1995.1004.

[17] I. Castro-Mateos, J.M. Pozo, T.F. Cootes, J.M. Wilkinson, R. Eastell, A.F. Frangi, Statistical Shape and Appearance Models in Osteoporosis, Curr. Osteoporos. Rep. 12 (2014) 163–173. https://doi.org/10.1007/s11914-014-0206-3.

[18] N. Sarkalkan, H. Weinans, A.A. Zadpoor, Statistical shape and appearance models of bones, Bone. 60 (2014) 129–140. https://doi.org/10.1016/j.bone.2013.12.006.

[19] B. Schuler, K.D. Fritscher, V. Kuhn, F. Eckstein, R. Schubert, Using a statistical appearance model to predict the fracture load of the proximal femur, in: M.I. Miga, K.H. Wong (Eds.), Med. Imaging 2009 Vis. Image-Guided Proced. Model., 2009: p. 72610W. https://doi.org/10.1117/12.811557.

[20] T. Whitmarsh, K.D. Fritscher, L. Humbert, L.M. del Río Barquero, T. Roth, C. Kammerlander, M. Blauth, R. Schubert, A.F. Frangi, Hip fracture discrimination from dual-energy X-ray

absorptiometry by statistical model registration, Bone. 51 (2012) 896–901. https://doi.org/10.1016/j.bone.2012.08.114.

[21] S.R. Goodyear, R.J. Barr, E. McCloskey, S. Alesci, R.M. Aspden, D.M. Reid, J.S. Gregory, Can we improve the prediction of hip fracture by assessing bone structure using shape and appearance modelling?, Bone. 53 (2013) 188–193. https://doi.org/10.1016/j.bone.2012.11.042.

[22] T.L. Bredbenner, R.L. Mason, L.M. Havill, E.S. Orwoll, D.P. Nicolella, Fracture Risk Predictions Based on Statistical Shape and Density Modeling of the Proximal Femur, J. Bone Miner. Res. 29 (2014) 2090–2100. https://doi.org/10.1002/jbmr.2241.

[23] H. Wold, Estimation of principal components and related models by iterative least squares, in: Multivar. Anal., 1966.

[24] R. Rosipal, N. Krämer, Overview and Recent Advances in Partial Least Squares, in: Lect. Notes Comput. Sci. (Including Subser. Lect. Notes Artif. Intell. Lect. Notes Bioinformatics), 2006: pp. 34–51. https://doi.org/10.1007/11752790_2.

[25] A. Aldieri, M. Terzini, G. Osella, A.M. Priola, A. Veltri, A. Angeli, A.L. Audenino, C. Bignardi, Osteoporotic Hip Fracture Prediction: Is T-Score-Based Criterion Enough? A Hip Structural Analysis-Based Model, J. Biomech. Eng. 140 (2018) 111004. https://doi.org/10.1115/1.4040586.

[26] M. Terzini, A. Aldieri, L. Rinaudo, G. Osella, A.L. Audenino, C. Bignardi, Improving the Hip Fracture Risk Prediction Through 2D Finite Element Models From DXA Images: Validation Against 3D Models, Front. Bioeng. Biotechnol. 7 (2019). https://doi.org/10.3389/fbioe.2019.00220.

[27] H.H. Bayraktar, E.F. Morgan, G.L. Niebur, G.E. Morris, E.K. Wong, T.M. Keaveny, Comparison of the elastic and yield properties of human femoral trabecular and cortical bone tissue, J. Biomech. 37 (2004) 27–35. https://doi.org/10.1016/S0021-9290(03)00257-4.

[28] E. Schileo, L. Balistreri, L. Grassi, L. Cristofolini, F. Taddei, To what extent can linear finite

element models of human femora predict failure under stance and fall loading configurations?, J. Biomech. 47 (2014) 3531–3538. https://doi.org/10.1016/j.jbiomech.2014.08.024.

[29] S. Durrleman, M. Prastawa, N. Charon, J.R. Korenberg, S. Joshi, G. Gerig, A. Trouvé, Morphometry of anatomical shape complexes with dense deformations and sparse parameters, Neuroimage. 101 (2014) 35–49. https://doi.org/10.1016/j.neuroimage.2014.06.043.

[30] M. Vaillant, J. Glaunès, Surface Matching via Currents, in: Lect. Notes Comput. Sci., 2005: pp. 381–392. https://doi.org/10.1007/11505730_32.

[31] S. Durrleman, X. Pennec, A. Trouvé, N. Ayache, Statistical models of sets of curves and surfaces based on currents, Med. Image Anal. 13 (2009) 793–808. https://doi.org/10.1016/j.media.2009.07.007.

[32] P. Gori, O. Colliot, L. Marrakchi-Kacem, Y. Worbe, C. Poupon, A. Hartmann, N. Ayache, S. Durrleman, A Bayesian framework for joint morphometry of surface and curve meshes in multi-object complexes, Med. Image Anal. (2017). https://doi.org/10.1016/j.media.2016.08.011.

[33] I.T. Jolliffe, J. Cadima, Principal component analysis: a review and recent developments, Philos. Trans. R. Soc. A Math. Phys. Eng. Sci. 374 (2016) 20150202. https://doi.org/10.1098/rsta.2015.0202.

[34] T.F. Cootes, G.J. Edwards, C.J. Taylor, Active appearance models, in: Lect. Notes Comput. Sci. (Including Subser. Lect. Notes Artif. Intell. Lect. Notes Bioinformatics), 1998: pp. 484–498. https://doi.org/10.1007/BFb0054760.

[35] T. Beck, Measuring the structural strength of bones with dual-energy X-ray absorptiometry: principles, technical limitations, and future possibilities, Osteoporos. Int. 14 (2003) 81–88. https://doi.org/10.1007/s00198-003-1478-0.

[36] A.A. Zadpoor, G. Campoli, H. Weinans, Neural network prediction of load from the morphology of trabecular bone, Appl. Math. Model. (2013). https://doi.org/10.1016/j.apm.2012.10.049.

[37] J.S. Gregory, D. Testi, A. Stewart, P.E. Undrill, D.M. Reid, R.M. Aspden, A method for

assessment of the shape of the proximal femur and its relationship to osteoporotic hip fracture, Osteoporos. Int. 15 (2004) 5–11. https://doi.org/10.1007/s00198-003-1451-y.

[38] J.C. Baker-LePain, K.R. Luker, J.A. Lynch, N. Parimi, M.C. Nevitt, N.E. Lane, Active shape modeling of the hip in the prediction of incident hip fracture, J. Bone Miner. Res. 26 (2011) 468–474. https://doi.org/10.1002/jbmr.254.